International Journal of Science and Research (IJSR)

ISSN: 2319-7064 Impact Factor 2024: 7.101

Environmental Current Pollution and Possible Interaction Mechanisms for Biological Effects

Kim Horsevad

Horsevad Independent Technical Research & Analysis, Tryvej 96, DK-9750 Denmark, www.horsevad.net Email: kim[at]horsevad.dk

Abstract: This paper addresses the emerging issue of environmental current pollution, offering systemwide estimates of stray currents originating from both centralized and decentralized power systems. Drawing on validated methodologies, the study develops models to quantify leakage from transmission lines, buried cables, and variable-frequency sources such as wind turbines. It further introduces a propagation framework that accounts for both resistive and capacitive effects in Earth's crust and atmosphere. Field measurements from magnetometer surveys and impedance studies support the model's accuracy. The paper also explores plausible biological effects, including DNA response elements, protein conformational shifts, and calcium channel modulation under low-frequency field exposure. The findings highlight the systemic presence and biological relevance of stray current pollution in modern power networks.

Keywords: Stray current, electromagnetic field, biological impact, environmental current pollution, leakage current propagation

1. Introduction

In an earlier study [1], we developed methodologies for quantifying stray currents at a single site. Building on these methods, it is now feasible to more robustly extend the analysis to a systemwide scale, enabling estimation of the total stray current emitted by a national transmission and distribution network.

2. Literature Survey

To the best of the author's knowledge, this is the first study to present a systemwide estimation of environmental current pollution.

3. Problem Definition

The aim of this study is to derive models for quantifying the systemwide magnitude of stray current leakage into the Earth from transmission and distribution infrastructure. These models are then applied to explore potentially relevant mechanisms of biological interaction arising from exposure to stray-current-induced electric, magnetic, and electromagnetic fields.

4. Methodology

Stray current from buried cables is estimated based on their cable-to-earth capacitance, enabling calculation of capacitive leakage. For overhead lines, leakage is modeled primarily through mutual inductive coupling to the shield or neutral conductors.

The combined magnitude of systemwide current pollution from both overhead and buried cables is then validated against field measurements.

In addition, a model is developed to estimate leakage from wind turbines and other VFD-based technologies, with results compared to practical measurements. Finally, the study outlines four biologically plausible mechanisms for biological effects of systemwide stray currents.

5. Results & Discussion

1) Estimating current pollution from buried cables We begin by analyzing the capacitive leakage current from a buried AC transmission cable.

The instantaneous capacitor current is defined by:

$$i(t) = \frac{C \cdot dV(t)}{dt}$$

where C is capacitance and V(t) is the instantaneous voltage

For an AC source, $V(t) = V_m \sin(2\pi f t)$

the derivative is

$$\frac{dV}{dt} = 2\pi f V_m \cos(2\pi f t)$$

Substituting gives $i(t) = C 2\pi f V_m \cos(2\pi f t)$

The maximum current occurs when $cos(2\pi ft) = 1$, so: $I_{max} = 2\pi f V_m C$

For an RMS voltage V, the same derivation gives: $I_{rms} = 2\pi f V_{rms} C$

where f is the supply frequency, $V_{\rm rms}$ is the line-to-ground voltage, and C is the total cable-to-earth capacitance (capacitance per unit length × cable length).

Reference values for cable capacitance are listed in Table 1. For estimation, we use $C=0.25 \,\mu\text{F/km}$ as a conservative figure.

Impact Factor 2024: 7.101

Table 1: Relevant standards for buried transmission and distribution cables.

TWO IN THE VALLE CONTROL OF CONTR							
Standard	Voltage Range (AC)	Cable Type / Insulation	Typical Capacitance Range (μF/km)	Notes			
IEC 60502-1	0.6 kV - 1 kV	XLPE, PVC, etc.	0.2-0.3	Low voltage, industrial and port			
IEC 60840	30 kV - 150 kV	XLPE, buried cable	0.18-0.26	Medium voltage, land and urban buried infrastructure			
IEC 62067	150 kV – 500 kV	XLPE, EPR, buried cable	0.18-0.26	Includes 220 kV, 330 kV, 400 kV; new installations			
IEEE Std 400/1017	60~kV-400~kV	XLPE/EPR (diagnostic/measurement)	0.18-0.26	Used for acceptance testing & diagnostics			
AS/NZS 2802	Mining trailing	XLPE/EPR	0.3-0.5	Robust, for mining			
UL 1309	Marine shipboard	Various	0.1-0.4	Shipboard, offshore			

For a 200 kV cable, the line-to-ground voltage is:

$$V_{ph} = \frac{V}{\sqrt{3}} = \frac{200 \, kV}{\sqrt{3}} \approx 115 \, kV$$

Using this, the capacitive leakage current per phase for a 20 km cable is:

$$I = 2 \pi 50 Hz 115.5 kV \cdot (2.5 \times 10^{-10} F/m 20000 m)$$

 $\approx 181 A$

We note that this estimation is in very close agreement with actual measurements done with earlier published methodologies [1].

It should be noted that phase imbalance can significantly alter shield or earth currents, introducing resistive components beyond the purely capacitive case. The geometry of bonding for the cable's metallic screen also affects current distribution. At 50 Hz, soil permittivity has negligible influence, as capacitance is dominated by the cable dielectric. Thus, this method provides a reliable basis for systemwide estimates of environmental current pollution from buried cables.

2) Current pollution from overhead cables

For overhead transmission lines, capacitive leakage is typically much smaller than for buried cables because of the reduced cable-to-earth capacitance. Instead, the dominant mechanism is inductive coupling into the shield or neutral conductors.

If we consider only capacitive leakage, the current is: $I = 2\pi f V_{ph} C L$

where f is frequency, V_{ph} is phase-to-earth voltage, C is capacitance per unit length, and L is cable length.

We again note standards and manufacturer's data for capacitance estimations:

Table 2: Relevant standards for overhead transmission and distribution cables.

Standard/Reference	Voltage Range (AC)	Cable Type / Insulation	Typical Capacitance Range (μF/km)	Notes
IEEE 1863 / IEC 60826	110–400 kV	Overhead transmission, ACSR/AAAC	0.007-0.01	Standard range for phase-to-earth; depends on geometry and height
Classic Texts & EE Curricula	11–132 kV	Overhead/uninsulated	0.006-0.009	Widely cited in academic & design references
Practical Engineering Guides	0.4–33 kV	Overhead distribution	0.006-0.008	Lower voltages, tighter pole spacing

For a 200 kV line with a 400 m span and C=0.0083 $\mu F/km = 8.3\times 10^{-12}~F/m$:

$$I = 2 \pi 50 Hz 115.5 \text{ kV} \cdot (8.3 \times 10^{-11} \text{ F/m } 400 \text{ m})$$

 $\approx 0.12 \text{ A}$

This estimation, however, is not in agreement with measured values done with earlier published methodologies [1], which show much higher currents.

Insulator leakage increases when surfaces are wet or polluted (e.g., salt, dust, industrial fallout). Typical strings carry microampere–milliampere levels, occasionally approaching sub-ampere currents on heavily contaminated 200 kV lines under high humidity. While these paths contribute to total leakage, they usually cannot explain multi-ampere ground currents by themselves.

At \sim 200 kV, corona onset is common. Ionized air increases the conductivity of the air–earth path, effectively adding a

resistive component. A standard engineering estimate for corona power per conductor length is given by Peek's law:

$$P_c = 242.4 (f + 25) \sqrt{\frac{r}{R}} (V_{ph} - V_d)^2 \cdot 10^{-5}$$

with f in Hz, V_{ph} and V_d in kV (rms, phase-to-earth), – Output P_c in kW per km per phase and r (conductor radius) and R (phase spacing) in the same length unit (commonly cm).

Even in heavy-corona conditions (e.g., ~5 kW/km), the implied discharge currents are typically sub-ampere, so corona alone does not account for the multi-ampere ground injections observed at pylons.

Even in a well-balanced three-phase system, the shield/ground wires and earth paths may carry induced circulating currents. Pylons can act as injection points for these currents into the earth, as these typically are grounded very well and bonded to the grounded shield wire (earth wire) running along the top..

Impact Factor 2024: 7.101

The ground wire is a conductor running parallel to the phase conductors. It is grounded at every pylon, so it forms a multigrounded line with distributed grounding. The alternating currents in the phase conductors induce an alternating voltage in the shield wire due to magnetic coupling.

The dominant mechanism is mutual inductive coupling from the phase conductors into the shield/ground wire that is bonded to earth at each pylon. The induced emf per unit length in the shield wire is

$$e_m = j \omega M I_n$$

where Ip is the phase current and M the mutual inductance per unit length and $\omega = 2\pi f$. Over a span of length d:

$$V_{ind} = j \omega M I_{p} d$$

For parallel conductors, the mutual inductance M (H/m) is given by:

$$M = \frac{\mu_0}{2\pi} \ln \frac{D}{h}$$

with D the horizontal separation between the phase bundle and the ground wire, and h the ground-wire height above earth. The approximate ground current injected at each pylon is then

$$I_g \approx \frac{\omega M I_\rho d}{R_a}$$

where $\omega = 2\pi f$, R_g is the pylon grounding resistance. For typical transmission parameters (e.g., I_p in the 100s of amperes, d~300–500 m, $Rg\sim2-10\,\Omega$), this model predicts ~5–20 A per pylon, consistent with field measurements. Unbalance and harmonics can further increase these currents.

3) Combined current pollution from transmission infrastructure

In Denmark, the transmission system is operated by Energinet. Publicly available figures [2] indicate that roughly 25% of high-voltage (132–400 kV) lines are underground, with the remainder overhead. The medium-voltage (10–60 kV) system contains both overhead and underground sections (in 2014, ~40% of 50–60 kV was underground), and most sub-10 kV networks are buried. Historical data suggest tens of thousands of kilometers of 10–20 kV lines remain in service. These figures allow a back-of-the-envelope systemwide estimate of stray current leakage contributions.

Overhead high voltage (132–400 kV).

Shield/ground wires are bonded to earth at each pylon. As derived above, typical shield-wire grounding currents are 5–20 A per pylon. With \sim 400 m span length, there are \sim 2.5 pylons/km, implying \sim 12.5–50 A/km aggregate leakage. Over, for example, \sim 5,000 km of overhead HV lines, this yields a total of \sim 60,000–250,000 A.

Medium-voltage (10-50 kV) overhead.

Induced currents per structure are smaller—on the order of 0.1-1 A. Assuming $\sim 50,000$ structures at an average 0.5 A, the aggregate is $\sim 25,000$ A.

Buried medium voltage (10–60 kV).

Capacitive leakage is the dominant mechanism, commonly $\sim 0.2-0.5$ A/km per phase. Using a conservative effective figure of ~ 0.3 A/km at the circuit level (after interphase cancellation and typical screen bonding), and $\sim 60,000$ km of underground MV cable, gives $\sim 18,000$ A.

Lower-voltage urban/residential (<10 kV).

Predominantly underground; per-kilometer capacitive leakage is small, with systemwide totals likely only a few hundred amperes.

Systemwide sum.

Adding the categories above gives a central estimate of $\sim 100,000$ A total stray current, with a plausible range of $\sim 50-300$ kA depending on actual line lengths, grounding resistance, phase unbalance/harmonics, soil resistivity, and seasonal loading. Relative to Denmark's land area ($\sim 43,000$ km²), this corresponds to an average areal current density on the order of a few amperes per km² ($\approx 2-3$ A/km² at 100 kA), noting that real-world distributions are heterogeneous and infrastructure-proximal regions are higher.

4) Validating transmission current pollution estimation by field measurements

For a large-scale leakage-current network, leakage is distributed rather than concentrated along a single line source. At distances far from any local pylon or buried cable (hundreds of meters to kilometers), the observed field is the superposition of many distant current sources. This produces a relatively uniform low-frequency magnetic background with a characteristic spectral peak at 50 Hz and harmonics.

Measuring this background allows estimation of an average underground current density J (A/m²). Modeling the current-carrying subsurface as a uniform horizontal sheet (effective thickness t, depth d), the vertical magnetic flux density above it can be approximated by the Biot–Savart relation:

$$B \approx \frac{\mu_0}{2} Jt$$

Two sites in Denmark were selected to bracket realistic conditions. Site 1 lies near the geographical center of Denmark (higher infrastructure density, "worst-case"); Site 2 lies in a remote rural area of Northern Jutland ("best-case").

At each site, a 10×10 m grid (1 m spacing) was surveyed for the AC magnetic field in the Z-axis using an IDR-322 (Integrity Design, Vermont, USA) calibrated precision single-axis magnetometer in AC mode, using earlier published magnetometer methodology [1]. Subsurface characterization used Schlumberger arrays and confirmatory digging where relevant to estimate layer depth and thickness.

Site 1 (infrastructure-proximal)

The principal current-carrying stratum was located at \sim 2 m depth with an effective thickness of \sim 0.5 m. The 100-point Z-axis measurements (see Figure 1) yielded an average underground current density of 6.1 A/m², which is several orders of magnitude above purely capacitive theoretical estimates for comparable separations from infrastructure.

Impact Factor 2024: 7.101

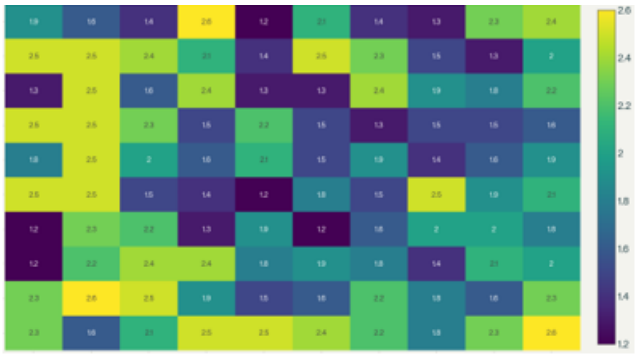


Figure 1: Heatmap visualization for the magnetometer readings at the first site. Measurements are taken in a 10m x matrix. All values are in μT . Minimum value 1.2 μT , maximum value 2.6 μT . The average is 1.93 μT and the standard deviation is 0.41.

Site 2 (remote).

The conductive stratum was ~5 m below ground and ~1 m thick (per Schlumberger array interpretation). The 100-point Z-axis measurements (see Figure 2) yielded an average underground current density of 0.008 A/m². Although much lower than Site 1, this "best-case" still exceeds the simplest theoretical estimates for capacitive coupling alone.

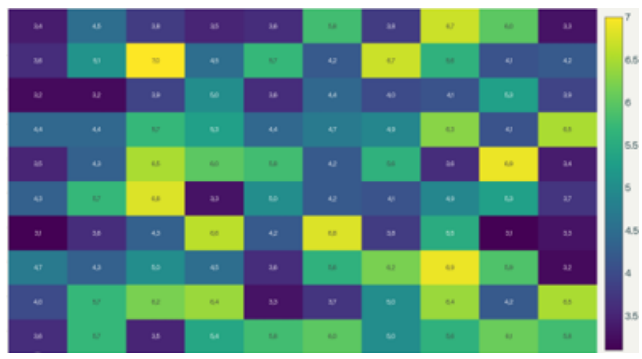


Figure 2: Heatmap visualization for the magnetometer readings at the second site. Measurements are taken in a 10m x matrix. All values are in nT. Minimum value 3.1 nT, maximum value 7.0 nT. The average is 4.83 nT and the standard deviation is 1.07.

The contrast between Site 1 and Site 2 illustrates the strong influence of nearby transmission/distribution infrastructure on environmental current pollution. Importantly, even the rural site exhibits measurable current density above purely theoretical baseline predictions, supporting the need to incorporate additional mechanisms (e.g., inductive shieldwire coupling, multi-grounded neutrals, return-current sharing through parallel metallic paths, and Earth—ionosphere capacitive shunting) in systemwide models.

Field voltages measured between conventional surface earth rods seldom exceed ~10 V, despite inferred underground currents that can be large (e.g., ~140 A total across multiple paths reported in [1]). This is reconciled by (i) low potential gradients along high-conductivity underground paths; (ii) limited coupling from deep conductive layers to surface probes; and (iii) the absence of a well-defined distant reference electrode. Consequently, surface inter-electrode voltages tend to underestimate the true subsurface potentials, whereas Z-axis magnetic surveys and surface electric-field measurements (commonly 20–50 V/m near strong

underground paths) are more sensitive indicators of high-current strata.

The measured Z-axis magnetic fields and inferred current densities at both sites are consistent with the combined leakage mechanisms developed in Sections A–C and the frequency-dependent propagation model of Section G. The agreement—particularly the elevated values near infrastructure and the non-zero background at a remote site—provides independent, field-based support for the systemwide leakage-current estimates.

5) Current pollution from return current

In earlier publications [3–5], values between 65% and 75% were reported for the portion of return current flowing through the earth rather than through dedicated conductors. While historically informative, such figures predate today's highly complex generation and distribution architectures and should not be generalized without caution.

In modern networks, the split between neutral-conductor return and earth/parallel-path return is inherently feeder-specific and varies over time. The partition depends on multiple interacting factors, including (but not limited to): soil resistivity and seasonal moisture variation; the density, impedance, and spacing of grounding electrodes; PEN integrity and continuity in TN-C-S/PME systems; load unbalance and harmonic content (which can raise neutral potentials and drive additional stray paths); and the presence of parallel metallic conductors (e.g., water and gas mains, district-heating pipes, lightning protection systems, rail infrastructure), as well as the proliferation of power electronics (e.g., EV chargers and VFDs) that introduce leakage through filters and parasitic capacitances.

In Denmark, urban areas are predominantly TN-C-S/TN-S. Multiple earthing (PME-style) combined with extensive buried metallic infrastructure creates numerous low-impedance parallel earth paths. Consequently, the earth-return component is non-trivial even where neutrals are healthy and well dimensioned. The actual fraction of current returning via earth therefore cannot be represented by a single universal percentage; rather, it depends on local topology, grounding practice, soil conditions, and load dynamics, and can change diurnally and seasonally.

From a practical standpoint, system operators and researchers should expect significant feeder-to-feeder variability. Meaningful quantification typically requires feeder-level measurements (e.g., neutral-to-earth voltage and current logging at multiple points, clamp-on assessments of downleads and bonding connections, and harmonic/resonance surveys) or circuit-specific modeling that explicitly includes neutral/earth bonding, parallel metallic paths, and realistic load spectra. These considerations explain why aggregated systemwide estimates—while useful—must be interpreted alongside local measurements to understand return-current behavior in a given area.

The pronounced contrast in magnetometer-derived current densities between the infrastructure-proximal and remote sites (Section D) underscores the necessity of location-

Impact Factor 2024: 7.101

specific measurements when characterizing earth-return and stray-current pathways.

6) Current pollution from Wind Turbines

Modern wind turbines use either doubly-fed induction generators (DFIG) with partial converters or full-converter machines (permanent-magnet or induction). In both cases, fast IGBT/SiC switching produces a common-mode voltage vcm(t) between the machine/cables and ground. This common-mode excitation acts across a large equivalent capacitance to ground, driving displacement currents.

The equivalent capacitance Ceq is the lumped sum of dominant paths:

- Stator/rotor-to-frame capacitance,
- Phase-to-shield/ground capacitance of tower/down-tower
- Output-filter and EMC Y-capacitors to ground,
- Transformer winding/screen stray capacitance to ground,
- Any array/export-cable capacitance effectively tied (directly or via screen) to station ground.

The common-mode displacement current and per-edge peak can be estimated. Fast PWM edges yield displacement current according to:

$$I_{cm}(t) = C_{eq} \frac{dV_{cm}}{dt}$$

The peak current per switching edge is:

$$I_{peak} = C_{eq} \left(\frac{dv}{dt} \right)$$

Each of the three legs contributes rise and fall events; a practical count is:

With rise time t_r, the duty factor (D) of the narrow spikes is:

$$D = N \cdot t_r \approx 6 f_{sw} \cdot t_r$$

Because the spikes are narrow, it is convenient to convert them to an RMS equivalent using the duty factor D.

Rectangular-pulse upper bound: $I_{ms,rect} = I_{peak} \sqrt{D}$

$$I_{ms,rect} = I_{neck} \sqrt{D}$$

Triangular-pulse lower bound (often closer to measured shapes):

$$I_{rms,tri} = I_{peak} \sqrt{\frac{D}{3}}$$

The rectangular case is a conservative upper bound; measured spectra and time-domain traces typically sit closer to the triangular lower bound due to finite device/loop dynamics and filtering.

A compact expression with shape factor $k_s \in [1/\sqrt{3},1]$ (triangular \rightarrow rectangular) is:

$$I_{rms} \approx I_{peak} \sqrt{k_s^2 D}$$

The PWM edge rate (dv/dt) can be of considerable magnitude, as two-level converters routinely hit 3–10 kV/µs edge rates, while SiC-based technologies can be yet higher.

Using the two bounding values for C_{eq} two illustrative examples can be worked:

For local (excluding array cables) and
$$C_{eq}=50$$
 nF $I_{peak}=50\times10^{-9}\cdot5\times10^{9}\approx250$ A per edge.

If array cables are included,
$$C_{\rm eq}$$
=0.2 μF
 $I_{\it peak}$ = 0.2× 10⁻⁶ ·5× 10⁹≈ 1000 $\it A$ per edge

For $f_{sw}=2$ kHz, $t_r=100$ ns, the duty factor is:

$$D = 6f_{sw}t_r = 6\ 2000\ 100 \times 10^{-9} = 0.0012$$

Upper bound of RMS leakage, using rectangular waveshape, and calculating for both local and arraycable-included scenarios:

$$I_{ms,rect}$$
= 250 $\sqrt{0.0012}$ ≈ 8.7 A
 $I_{ms,rect}$ = 1000 $\sqrt{0.0012}$ ≈ 34.6 A

Lower bound of RMS leakage, using triangular waveshape, and calculating for both local and arraycable-included scenarios:

$$I_{ms,tri}$$
= 250 $\sqrt{0.0012/3} \approx 5.0 A$
 $I_{ms,tri}$ = 1000 $\sqrt{0.0012/3} \approx 20.0 A$

In Denmark there are ~4,000 wind turbines; thus, even modest per-turbine leakage becomes system-relevant when aggregated. The exact injection pathways (tower bonding, filter topology, transformer screen grounding, array-cable screening and terminations) determine how much of the common-mode current returns via earth versus shield/structural loops, but the net leak to ground is non-trivial at the fleet level.

7) Stray current propagation

Estimating propagation of stray current from far-away sources through the Earth requires a reliable estimate of the effective impedance experienced by the current over distance.

Unlike a traditional cable, where the geometry and material properties are well-defined, the Earth presents a complex, multi-path medium where current spreads radially through inhomogeneous strata.

The goal is to estimate the effective impedance experienced by a stray current I_{src} injected into the Earth, as it propagates through the subsurface medium and returns via remote ground paths or infrastructure coupling. The impedance model must account for both resistive conduction and frequencydependent capacitive coupling.

Impact Factor 2024: 7.101

In a homogeneous, isotropic medium, the resistance between a point source and remote ground at a distance D can be approximated by:

$$R(D) = \frac{\rho}{2\pi D}$$

where:

- ρ is the soil resistivity $|\Omega \cdot m|$,
- D is the distance from the source [m].

For convenience, we define a reference resistance R₀ corresponding to a standard distance D₀ and reference resistivity ρ_{ref} . The general resistive term then becomes:

$$R(D) = R_0 \cdot \left(\frac{\rho}{\rho_{ref}}\right) \cdot \left(\frac{D}{D_0}\right)$$

The Earth and ionosphere form a large spherical parallel-plate capacitor. For a circular area of radius D, the capacitance is approximated as:

$$C_{\text{eff}}(D) = \epsilon_0 \epsilon_r \frac{\pi D^2}{H}$$

where:

- ϵ_0 = vacuum permittivity = 8.85×10⁻¹²F/m,
- $\epsilon_{\rm r} \approx 1$ for air,
- H≈80km is the ionosphere height.

This gives rise to a frequency-dependent capacitive reactance:
$$X_{\rm C}(D,f) = \frac{1}{2\pi f \, C_{\rm eff}(D)} \propto \frac{H}{f \, D^2}$$

circuit:

$$Z_{eff}(D,f) = \left(\frac{1}{R(D)} + j2\pi f C_{eff}(D)\right)^{-1}$$

Taking the magnitude:

$$|Z_{eff}(D,f)| = \frac{R(D)}{\sqrt{1 + (2\pi f R(D)C_{eff}(D))^2}}$$

Substituting the empirical forms and gathering constants into a single fitted parameter k2 yields the working model used throughout:

$$|Z_{eff}(D,f)| = \frac{R_0(\rho/\rho_{ref})(D/D_0)}{\sqrt{1+(2\pi f D k_2)^2}}$$

Where:

- R₀=base resistance at reference conditions
- p: site-specific resistivity $[\Omega \cdot m]$
- $\rho_{ref} = 100 \Omega \cdot m$
- f: frequency (Hz)
- D: distance (km)
- k₂=frequency-scaling parameter tied to Earth-ionosphere capacitive coupling

To identify R₀ and k₂, we performed controlled injectionreception measurements at a fixed path length D₀=1 km in moist clay (assumed $\rho_{ref}=100 \ \Omega \cdot m$). For each frequency f, we measured the total impedance |Z(f)|, inferred C(f), and computed XC(f)= $1/(2\pi fC(f))$.

The table below summarizes the collected data:

Table 3: Measurements from the injection-reception impedance measurement experiment. Accuracy of the measured impedance is down to $10m\Omega$, accuracy of the capacitance measurements is better than 10μF/F

Frequency (Hz)	Capacitive Reactance XC (Ω)	Capacitance (μF)	Measured Impedance $Z(\Omega)$
50	52	60	979
100	38	40	968
200	35	23	957
400	39	10	946
800	28	7	937

At D=D₀ and ρ = ρ_{ref} , the model reduces to

$$|Z(f)| = \frac{R_0}{\sqrt{1 + (k_2 f)^2}}$$

A nonlinear least-squares fit gave:

$$R_0 \approx 945.7 \,\Omega$$
, $k_2 \approx 3.17 \times 10^{-5} \,\text{s/km}$

The fit matches the measured values from 50-800 Hz with residuals within $\pm 1\%$, supporting the parallel conduction capacitance picture over ELF/low-VLF bands.

R₀ represents the effective resistive component of the Earth at 1 km under reference conditions (ρ =100 Ω ·m).

k₂ captures the influence of Earth-ionosphere capacitive coupling and implicitly reflects the effective height of the ionospheric return path. The value is consistent with a capacitive shunt formed over an ionospheric gap of ~80km, and matches estimates derived from parallel-plate capacitance formulas:

$$C_{eff} \approx \frac{\epsilon_0 \pi D^2}{H}$$

Combined, this provides the mathematical foundation to model the Earth as a a distributed medium with both conductive and capacitive components. For frequencies in the ELF and low VLF range (10 Hz - 1 kHz), the total effective impedance between a source and a remote point can be described as a parallel combination of a series resistive conduction path through the Earth's crust, scaling with resistivity ρ and distance D and a capacitive path representing the Earth-ionosphere cavity, with capacitance scaling with the surface area subtended by the source and receiver.

For the Low-frequency / conduction-dominated regime we can write:

$$|Z_{eff}(D, f)| \approx R_0 \left(\frac{\rho}{\rho_{ref}}\right) \left(\frac{D}{D_0}\right)$$

This regime reflects path-following conduction, consistent with extended strata and utility corridors.

For the high-frequency / capacitive shunting regime we can write:

$$|Z_{eff}(D,f)| \approx \frac{R_0}{2\pi f k_2} \left(\frac{\rho}{\rho_{ref}}\right)$$

Notably, the high-frequency limit is approximately distanceindependent, because capacitive coupling to the ionosphere dominates long-range return.

Volume 14 Issue 10, October 2025 Fully Refereed | Open Access | Double Blind Peer Reviewed Journal www.ijsr.net

Paper ID: SR251005215821

Impact Factor 2024: 7.101

As D increase such that $2\pi fDk_2 \ge 1$, the denominator term grows and |Zeff| flattens with distance. This explains how ELF/low-VLF leakage can propagate efficiently over very long ranges with modest incremental attenuation.

This model accurately predicts attenuation of low-frequency currents over long distances and transitions smoothly between the resistive (low-frequency) and capacitive (high-frequency) regimes.

According to the model, absolute voltages at the point of injection may reach hundreds of volts relative to distant Earth potential. However, these voltages are not directly observable with conventional surface probes due to limited coupling and the absence of a defined remote ground reference. The model estimates absolute voltage relative to the injection site, while practical measurements reflect only local potential differences between accessible surface locations.

In the field, potential differences measured between standard earth rods will therefore generally underestimate the true underground potential.

Instead, surface electric field measurements can serve as reliable indicators of buried high-current paths, even when inter-electrode voltages are low. Measurements between 20 and 50 V/m are commonly observed in vicinity of such underground current paths.

The practical implication of this is the understanding that stray current, once injected into the ground, effectively can propagate nearly unattenuated for continental distances

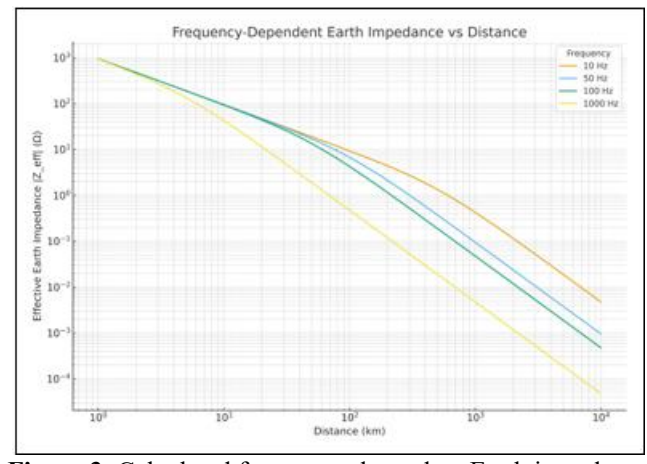


Figure 3: Calculated frequency-dependent Earth impedance vs distance.

At short distances (1–10 km), impedance is dominated by resistive conduction, decreasing approximately as 1/D. Beyond hundreds of kilometers, the curve flattens, reflecting the increasing dominance of capacitive shunting via the Earth-ionosphere cavity. The asymptotic flattening at long distances implies that stray current signals can propagate efficiently over global scales without linear attenuation.

This is often utilized by the WSPR radio amateur community, where cross-continental reception of sub-watt-transmissions via ground rods is routinely reported.

It should be noted that the the derived model used here is not an exact electrodynamic model of the Earth-ionosphere cavity.

It is an effective stray-current propagation model, derived from controlled injection–reception data, that reproduces the observed distance–frequency behavior and reveals that significant current transport can occur over continental distances at ELF/low-VLF.

A naive spherical or parallel-plate estimate of Earth–ionosphere capacitance, with ϵ_0 = 8.85×10^{-12} F/m, yields values that are orders of magnitude below the empirical shunt implied by the fitted parameter k_2 . This discrepancy is expected because the parallel plate or spherical models assumes uniform gap and homogeneous field lines, neither of which holds in real environments affected by stray currents. What the fitted shunt represents is an apparent (effective) capacitance per distance, arising from many distributed pathways:

- Soil inhomogeneity and anisotropy. Layered clays, tills, and aquifers create guided current paths and Maxwell– Wagner interfacial polarization, producing large, frequency-dependent effective permittivities (αdispersion) and boosting apparent capacitive coupling.
- Atmospheric conductivity gradient. The lower atmosphere
 is not a perfect dielectric plate; conductivity increases with
 altitude. Quasi-static displacement and leakage
 conduction share the return, bending field lines and
 compressing the effective gap over the
 distances/frequencies used here.
- Lateral conduction and "near-return" shortcuts. Return
 paths are not purely vertical to the ionosphere: nearby
 infrastructure (multigrounded neutrals, pipelines, districtheating mains, rails, LPS down conductors,
 tower/structure networks) and surface/near-surface
 moisture provide parallel shunts that behave like added
 capacitance in the aggregate model.
- Environmental and transient effects. Seasonal moisture, groundwater level, precipitation wetting, surface films, vegetation water content, space charge/corona ions, and pollution layers all increase effective coupling intermittently or persistently.
- Geometric saturation of field aperture. The effective "area" participating in the return does not grow as D² as in the ideal plate; it tends to saturate or grow subquadratically because current follows conductive corridors and field lines crowd into the lowest-impedance routes.

Mathematically, our fitted form should therefore be interpreted as a phenomenological RC network surrogate, where k_2 conflates several effects into a single, reproducible distance—frequency trade-off. It should not be confused with a claim on the literal capacitance of the Earth—ionosphere cavity. Instead, the "capacitance" in this work is an effective shunt emerging from a distributed, frequency-dispersive environment (heterogeneous soils + atmospheric/leakage + infrastructure coupling). The parallel-plate formula is too idealized for this context; our fitted model purposefully captures the aggregate pathway that best explains the observed propagation of stray currents

International Journal of Science and Research (IJSR)

ISSN: 2319-7064 **Impact Factor 2024: 7.101**

Mechanisms for biological effects

Possible biological effects from electric, magnetic, and electromagnetic fields at non-thermal intensities constitute a large research domain with considerable volume but limited consensus. To avoid adjudicating competing claims, the present study does not attempt a comprehensive review. Instead, it highlights mechanisms that are plausibly relevant under stray-current exposure scenarios, setting the stage for the specific molecular/cellular routes discussed in Sections I-

When a biological system is exposed to an external field, a displacement current can flow through the body's effective capacitance to its surroundings. The basic relation is

$$I_d = C_{body} \frac{dV}{dt} = 2\pi f C_{body} V_{eff}$$

where C_{body} is the body-to-ground (or body-to-environment) capacitance, f the frequency, and V_{eff} the effective potential difference (often well-approximated by field x height for quasi-uniform fields):

Typical standing human values are C_{body}≈100–300 pF (larger for pigs and cows, depending on posture, proximity to ground, surface moisture, and enclosure geometry). At 50 Hz and modest environmental field levels, the resulting I_d is generally in the μ A range; at higher frequencies, the $2\pi f$ factor can, in theory, drive I_d toward mA levels. However, such upperbound calculations should be interpreted cautiously: realistic absorption cross-sections, dielectric dispersion of skin/tissue, non-uniform fields, and imperfect coupling all act to reduce the raw numbers, especially above ELF/low-VLF.

That said, broadband EMC noise from power-electronics (e.g., VFDs in wind turbines) can extend far beyond 50-60 Hz (often with spectral content up to the MHz range). In such environments—even when the acute risk is low—chronic exposure remains under-researched, and conservative evaluation is warranted.

In Danish industrial-scale farms, floors are typically reinforced concrete; in some areas, closely spaced steel bars are used and bonded to earth with low impedance. This changes the coupling dramatically: instead of a purely capacitive path (hundreds of $k\Omega$ at \sim MHz for a free-standing body), the animal-ground path becomes resistive + capacitive, with effective impedances that can drop to tens of Ω to $k\Omega$ depending on hoof conductivity and moisture.

Under such conditions, any available potential difference between the animal and the grounded floor can drive conduction current in addition to displacement current.

In practice, this means that μA to mA levels of 50 Hz (and harmonic) currents are possible—and have been observed in field measurements—via the floor/structure return paths.

The estimates above are order-of-magnitude guides. Actual I_d and conduction currents depend on local geometry, posture, surface conditions, materials, and frequency content (including harmonics/EMC noise).

This mechanism is often overlooked when exposures are evaluated solely through air-gap field strengths or inter-rod voltages at the surface; yet it can dominate the bio-relevant current that actually traverses an animal or human body in grounded settings.

A related epidemiological consideration is that contact currents as low as ~18 µA have been reported in association with cancer risk in residential contexts [6]. While causality is debated and context differs, the magnitudes are well within what farm environments can sustain under the resistive + capacitive coupling described above.

For grounded environments, surface electric-field mapping (along with clamp-on measurements of down-leads/bonding conductors where feasible) provides a more faithful indication of bio-relevant currents than relying on surface inter-rod voltages alone — which can underestimate subsurface potentials and bypass currents.

9) Electromagnetic response elements in DNA

To evaluate the biological significance of environmental current pollution, it is necessary to consider plausible molecular routes by which electromagnetic fields (EMFs) can influence living systems. A central line of evidence comes from work by Martin Blank and Reba Goodman, who identified specific electromagnetic response elements (EMREs) in DNA that act as field-sensitive promoter elements—challenging the earlier assumption that DNA is electromagnetically inert at non-thermal field strengths [7,8,9].

Blank and Goodman reported a consensus nCTCTn motif (n any nucleotide) as an EMRE that confers EMF responsiveness to certain promoters:

- HSP70 promoter. Three nCTCTn elements lie between 230 and -160 relative to the transcription start site; this EMF-responsive region is functionally distinct from the heat-shock domain at -111 to -67. Deleting the 70-bp segment containing the three nCTCTn sites abolished **EMF** responsiveness while preserving thermal responsiveness.
- c-myc promoter. Eight nCTCTn elements are distributed across a ~900-bp segment (-1257 to -353). When this segment was placed upstream of CAT or luciferase reporters—otherwise unresponsive to EMFs—HeLa cells exposed to 8 µT, 60 Hz for 30 minutes showed significant increases in reporter activity compared with sham.

To explain promoter-level sensitivity, Blank and Goodman proposed that ELF fields perturb electron transfer within DNA: mobile electrons (notably those involved in hydrogen bonds between base pairs) are displaced by applied fields, producing transiently charged groups at nCTCTn sites. The resulting local destabilization can favor base-pair separation, facilitating initiation of transcription. Although electron and hydration dynamics occur at much higher intrinsic frequencies, ELF oscillations can act as quasi-static, pulselike perturbations in this context.

In later work [9], the same authors proposed that DNA may behave as a fractal antenna—combining electronic conduction along the double helix with hierarchical self-

Impact Factor 2024: 7.101

symmetry—thereby enabling interactions across a broad frequency range (ELF through RF). This framework was advanced to rationalize reports that both ELF and RF fields can induce similar biological responses (e.g., stress-protein expression, strand breaks). While the idea is sits beyond the scope of our modeling, we note it here as a unifying hypothesis consistent with their promoter findings.

Our mention of EMREs is hypothesis-driven and mechanistic: these promoter elements provide a concrete, gene-regulatory route by which weak, non-thermal fields—of the kind associated with stray-current environments—could modulate transcription. We make no claim that EMREs constitute the sole or dominant pathway in all contexts; rather, they are a plausible, experimentally supported mechanism that complements the additional routes discussed in Sections J-K.

10) Wring resonances

Whereas covalent bonds are too strong to be directly influenced by the stray-current-induced fields discussed in this study, most three-dimensional conformations of biological macromolecules (e.g., proteins) are stabilized by weaker interactions-van der Waals forces, London dispersion, hydrogen bonds, and related noncovalent effects—that can, in principle, be perturbed at much lower energy.

One such mechanism is the wring resonance (terminology as used in [10–12]), examined in a set of theoretical studies from 1997 that presented a detailed and rigorous mathematical model of how weak electromagnetic waves could influence macromolecular conformational stability via local resonance amplification [10-12]. A few years later, the research group reported experimental validation consistent with the theoretical predictions [13,14].

Most resonance frequencies analyzed in the original theoretical work lie above what is typically considered for classical "stray current" exposures. However, the continual push toward higher efficiency in variable-frequency drives (VFDs) raises harmonic and broadband noise content to progressively higher frequencies. As a result, exposure spectra in practical settings—particularly near large-scale power electronics—can overlap with the frequency ranges evaluated in the wring-resonance framework, making these studies relevant to the present exposure scenarios.

11) Schwan-driven modulation of VGCC-gating

The idea that non-thermal electromagnetic fields can modulate voltage-gated calcium channels (VGCCs) was first articulated by Dimitris J. Panagopoulos and colleagues [15]-[17] and subsequently experimentally verified a number of times [18]-[20].

Their work framed VGCCs—particularly L-type channels as sensitive transducers whose voltage-sensor domains could be biased by weak external fields, thereby altering open probability and downstream Ca²⁺-dependent signaling.

In this section, we retain that biological hypothesis while presenting a general, quantitative derivation based on classical Schwan-type membrane polarization. The aim is not to replace the original insight, but to strengthen it by providing a transparent bridge from applied field → membrane polarization -> gating energetics, so that assumptions and scaling are explicit.

A uniform external field induces a position-dependent transmembrane voltage across a spherical cell of radius a.

The frequency-domain Schwan relation is:

$$\Delta V_m(\theta,\omega) = \frac{3}{2} a E(\omega) \cos\theta K(\omega)$$

where $E(\omega)$ is the external electric field amplitude, $\cos\theta$ the angle θ relative to field direction and where the dispersion factor

$$K(\omega) = \frac{1}{\sqrt{1 + (\omega \tau_m)^2}}$$

captures membrane charging with time constant

$$\tau_m = aC_m(\rho_i + \rho_e)$$

Polarization is maximal at the poles $(\theta=0,\pi)$ and zero at the equator. Microgeometry (folds, junctions, microvilli) can locally concentrate fields; we represent this by a geometric

$$\Delta V'_{m} = G_{\vec{E}} \Delta V_{m}$$

A small voltage shift changes VGCC energetics by $\Delta U_{\text{field}} = zq\Delta V'_{\text{m}}$ (effective gating charge z, elementary charge q). Linearizing the Boltzmann activation around mid-slope

$$\Delta P \approx \frac{1}{4} \frac{zq}{k_B T} \Delta V'_m$$

with $k_BT/q\approx 25.7$ mV at room temperature.

For a cell of radius a=5 μm in a 30 V/m external field, and

$$\Delta V_m(pole) \approx \frac{3}{2} a E = \frac{3}{2} (5 \times 10^{-6}) 30 \approx 225 \mu V$$

Assuming GE=1 and z=4:

$$\Delta P \approx \frac{1}{4} \cdot \frac{4 \, q}{k_B T} \cdot (225 \, \mu V) = \frac{q}{k_B T} \cdot 225 \, \mu V$$

$$\approx \frac{0.225 \, mV}{25.7 \, mV} \approx 0.0087 \quad (0.87 \, \%)$$

With modest geometric concentration GE=2-3, $\Delta V'm$ and ΔP scale linearly, giving ~1-3% shifts—small but non-zero biases consistent with subtle modulation under chronic exposure.

Perfect isotropy would average $\cos\theta$ to zero, but channel clustering, fiber orientations, and microdomain structure create local hotspots. Bulk averages can underestimate biologically relevant local effects.

Schwan's formulation is linear and assumes a sphere; real cells deviate (shape anisotropy, dispersive C_m, heterogeneous

Impact Factor 2024: 7.101

sigma). The derived model give order-of-magnitude guidance; bounds can be explored via GE and z.

At higher frequencies, dispersion reduces effective ΔVm , while power-electronics spectra can add harmonics/EMC noise that warrant case-specific assessment. The VGCC linearization applies to small $\Delta Vm'$ near mid-activation; outside that range, the full Boltzmann form might be utilized to provide similar modelling.

With the above limitations in mind, this analysis indicates that low-frequency electric fields at levels commonly found near leaky transmission infrastructure can induce transmembrane polarization on the order of a few hundred microvolts—well below classical electroporation thresholds (\approx 0.2–1 V), yet sufficient to shift VGCC open probability by percent-level amounts.

6. Conclusion

This study develops and validates a practical framework for quantifying environmental current pollution from modern power systems. Starting from first principles, we derive leakage mechanisms for buried cables (capacitive), overhead lines (primarily inductive coupling into shield/ground wires), converter-based generation (common-mode displacement currents from VFDs in wind turbines). We then introduce an effective propagation model that captures the observed distance-frequency trade-off in the Earth, combining path-following conduction with an empirical shunt that represents distributed capacitive/leakage returns. The model is anchored to field data (magnetometer surveys, Schlumberger arrays, and injection-reception measurements) and reproduces measured impedances across 50-800 Hz with small residuals.

At the infrastructure level, the analysis indicates non-trivial systemwide leakage. Typical values are on the order of 9 A/km for buried transmission segments and ~12.5–50 A/km for overhead lines (via shield-wire coupling), with per-pylon injections of ~5–20 A under representative parameters. Aggregated to national scale, a central estimate near 100 kA (with a plausible range of ~50–300 kA) emerges, consistent with independent field observations and with the spatial patterns seen in Z-axis magnetic maps. Importantly, measured surface voltages between casual probe points can remain modest (few–tens of volts) even when underground currents are large—underscoring that magnetometry and E-field mapping are often more faithful indicators of subsurface currents than inter-rod voltages alone.

On biological relevance, we outline plausible, mechanism-based routes by which the fields associated with stray currents may interact with living systems. In particular, Schwan-type membrane polarization at ELF can yield hundreds of microvolts of transmembrane shift—far below electroporation thresholds yet sufficient to bias VGCC open probability at percent-level magnitudes under realistic conditions. These estimates complement prior work on electromagnetic response elements in DNA and the wring-resonance framework at higher spectral content, without overstating any single pathway.

The scope of the propagation model is phenomenological: its shunt term is not a literal Earth—ionosphere capacitance but a data-fitted surrogate for distributed coupling through heterogeneous soils, atmospheric conductivity gradients, moisture-laden structures, and parallel metallic networks. As such, results should be interpreted alongside location-specific measurements; the contrast between infrastructure-proximal and remote sites in this study illustrates that local topology, grounding practice, and seasonal conditions materially affect outcomes.

Environmental current pollution is measurable, modelable, and materially significant at system scale. Recognizing and quantifying these currents matters for exposure assessment, infrastructure design (bonding, shielding, screen terminations, filter topology, transformer screen grounding), and mitigation near sensitive sites (e.g., large animal facilities, clinical/industrial laboratories).

A natural next step is to incorporate scale-dependent path multiplicity and anisotropic/layered conductivities into the resistive term, and to disaggregate the empirical shunt into atmosphere vs. infrastructure components via controlled experiments (e.g., seasonal wet/dry runs, tower-bonding toggles, neutral isolation trials, and targeted ELF injections along known corridors). We expect such refinements to reveal still lower attenuation at ELF and to further clarify the partitioning between neutral conductors, infrastructure loops, and true earth return.

7. Future Scope

The present framework demonstrates that environmental current pollution can be quantified, modeled, and validated against field data. Several lines of work would strengthen and extend these results:

OpenDSS-assisted inference can be used to bound ground-borne return currents without any direct access to transmission assets. Minimal feeder surrogates can be assembled from public sources and on-site observation—line voltages and approximate lengths, typical span geometry, presence of shield/neutral conductors, and representative grounding resistances—together with plausible ranges for load unbalance and harmonic content. These surrogate circuits permit scenario sweeps that predict per-pylon injections and areal current density under varied terminations and bonding strategies.

Crucially, the simulations can be calibrated against field measurements: two-dimensional Z-axis magnetic grids and co-registered surface E-field transects provide spatial patterns that can be matched, in a least-squares sense, by tuning a small set of parameters (e.g., average grounding resistance, degree of unbalance). Rather than over-claiming precision, the outcomes should be reported as credible intervals derived from the envelope of scenario fits, together with residual maps that show where models under- or over-predict measured fields.

Even under conservative assumptions, this workflow yields practically useful bounds on earth-return fractions and highlights the design choices (screen terminations, bonding

Impact Factor 2024: 7.101

layout, grounding values) most likely to influence perstructure injections.

Another relevant path would focus on increasing the accuracy of the stray current propagation model. The derived model for stray current propagation captures the observed distance—frequency trade-off using a phenomenological parallel R||C surrogate. It does not yet incorporate the geometric fact that, as the source—receiver separation grows, the number of available parallel conductors—both natural (clays, aquifers, saline lenses) and man-made (multigrounded neutrals, pipelines, rails, district-heating grids, LPS networks)—increases rapidly with scale. Intuitively, the "aperture" of potential return paths expands with the area/volume between the points, so the net parallel conductance increases with distance, counteracting simple 1/D attenuation.

A more complete conduction model would allow the effective conductivity to grow with the search radius, or, equivalently, allow the resistive term to drop with a path-multiplicity factor so the resistive part grows like $D^{1-\alpha}$ rather than D. When inserted in the parallel model, this yields an even flatter distance-dependence than our current fit—precisely the direction suggested by field experience at ELF/low-VLF. We have not used this refinement in the present fits; it is noted here to indicate the expected behavior of a fuller model.

Deep-layer participation further strengthens this tendency. At ELF, the skin depth

$$\Delta(f,\sigma) = \sqrt{\frac{2}{\mu_0 \sigma(2\pi f)}}$$

is hundreds to thousands of meters for typical soils. For example:

- σ =0.1 S/m (10 Ω ·m), f=50 Hz \rightarrow $\delta \approx 225$ m;
- σ =0.01 S/m (100 Ω ·m), f=50 Hz $\to \delta \approx 712$ m;
- σ =0.001 S/m (1k Ω ·m), f=50 Hz $\rightarrow \delta \approx 2.25$ km.

These depths are well beyond the reach of shallow arrays, meaning deeper, laterally extensive layers (and seawater boundaries) can act as low-impedance superhighways that widen the effective return aperture with distance. This also helps explain historical observations using VLF/ELF submarine transmitters (e.g., the Russian "ZEVS" at ~82 Hz): long-range ground returns imply large-scale, multi-path conductance that simple local models underpredict.

References

- [1] Horsevad, Kim. 2025. "Development of Differential Magnetic Field Methodology for Estimating Quantity of Stray Current Carried Through Conductive Earth", International Journal of Science and Research (IJSR), Volume 14 Issue 5, May 2025, pp. 793-798.
- [2] Wikipedia contributors. Electricity sector in Denmark. Wikipedia, The Free Encyclopedia. September 19, 2025, 08:53 UTC. Available at: https://en.wikipedia.org/w/index.php?title=Electricity _sector_in_Denmark&oldid=1312207653. Accessed October 2, 2025.
- [3] Morrison, C. 1963. "A Linear Approach to the Problem of Planning New Feed Through Points Into a Distribution System." AIEE Trans. III. (PAS) Dec. 1963 p 819-832

- [4] Hendrickson, R.C., Mike Michaud and Alvin Bierbaum. 1995. "Survey to Determine the Age and Condition of Electric Distribution Facilities in Minnesota: Report 1: Analysis of Overhead Distribution Feeder Testing Data". Minnesota Public Utilities Commission. May 18, 1995
- [5] Gonen, Turan. 1986. "Electric Power Distribution System Engineering". Hightown, NY: McGraw Hill
- [6] Kavet, R., Zaffanella, LE., Daigle, JP. and Ebi, KL. 2000. The possible role of contact current in cancer risk associated with residential magnetic fields. Bioelectromagnetics, 21: 538–553.
- [7] George I, Geddis MS, Lill Z, Lin H, Gomez T, Blank M, Oz MC, Goodman R. Myocardial function improved by electromagnetic field induction of stress protein hsp70. J Cell Physiol. 2008 Sep;216(3):816-23
- [8] Lin H, Blank M, Rossol-Haseroth K, Goodman R. Regulating genes with electromagnetic response elements. J Cell Biochem. 2001;81(1):143-8.
- [9] Blank M, Goodman R. DNA is a fractal antenna in electromagnetic fields. Int J Radiat Biol. 2011 Apr;87(4):409-15.
- [10] Bohr J, Bohr H. The implication of topology for protein structure and aggregation. Z. Physik D. 1997; 40:186-198
- [11] Bohr J, Bohr H, Brunak S.. Protein folding and wring resonances. Biophysical Chemistry 1997; 63:97-105
- [12] Bohr H, Brunak S, Bohr J. Molecular Wring Resonances in Chain Molecules. Bioelectromagnetics 1997; 18:187–189
- [13] Bohr H, Bohr J. Microwave Enchanced Kinetics Observed in ORD Studies of a Protein. Bioelectromagnetics 2000; 21:68-72
- [14] Bohr H, Bohr J, Microwave-enhanced folding and denaturation of globular proteins. Physical Review, 2000;61(4);4310-4314
- [15] Panagopoulos DJ, Messini N, Karabarbounis A, Filippetis AL, Margaritis LH. A Mechanism for Action of Oscillating Electric Fields on Cells. Biochemical and Biophysical Research Communications 2000;272(3):634-640.
- [16] Panagopoulos DJ, Karabarbounis A, Margaritis LH. Mechanism for Action of Electromagnetic Fields on Cells. Biochem. Biophys. Res. Commun 2002;298(1):95-102.
- [17] Panagopoulos DJ, Margaritis LH. Theoretical Considerations for the Biological Effects of Electromagnetic Fields. In: Stavroulakis P. (Ed.) Biological Effects of Electromagnetic Fields, Springer, 2003:5-33.
- [18] Panagopoulos DJ, Chavdoula ED and Margaritis LH. Bioeffects of Mobile Telephony Radiation in relation to its Intensity or Distance from the Antenna. International Journal of Radiation Biology 2010;86(5):345-357.
- [19] Panagopoulos DJ and Margaritis LH. Mobile Telephony Radiation Effects on Living Organisms, In: Harper AC, Buress RV. (Ed.) Mobile Telephones: Networks, Applications and Performance. Nova Science Publishers, 2008:107-149.
- [20] Panagopoulos DJ, Margaritis LH. Biological and Health effects of Mobile Telephony Radiations,

Impact Factor 2024: 7.101

International Journal of Medical and Biological Frontiers 2009;15(1-2):33-76.

Author Profile



Kim Horsevad is the founder and chief technical analyst at Horsevad Independent Technical Research & Analysis (www.horsevad.net). Current research focuses on developing methodologies for quantifying

on developing methodologies for quantifying interactions between electromagnetic fields and biological systems, with a particular emphasis on field-based diagnostics and practical mitigation strategies.